ACS APPLIED MATERIALS & INTERFACES

Letter

www.acsami.org

Voltage Controlled Hot Carrier Injection Enables Ohmic Contacts Using Au Island Metal Films on Ge

Srinivas Ganti,[†,‡] Peter J. King,[†,§,‡] Erhan Arac,[‡] Karl Dawson,[⊥] Mikko J. Heikkilä,[§] John H. Quilter,[∥] Billy Murdoch,[#] Peter Cumpson,[#] and Anthony O'Neill*[,‡]

[‡]School of Electrical and Electronic Engineering and [#]School of Mechanical and Systems Engineering, Newcastle University, Newcastle upon Tyne NE1 7RU, United Kingdom

[§]Department of Chemistry, University of Helsinki, A.I Virtasen aukio 1, Helsinki FI-00560, Finland

[⊥]Department of Mechanical, Materials and Aerospace Engineering, School of Engineering, University of Liverpool, Liverpool L69 3BX, United Kingdom

[∥]London Low Temperature Laboratory, Royal Holloway University of London, Egham TW20 0EX, United Kingdom

Supporting Information

ABSTRACT: We introduce a new approach to creating low-resistance metal−semiconductor ohmic contacts, illustrated using high conductivity Au island metal films (IMFs) on Ge, with hot carrier injection initiated at low applied voltage. The same metallization process simultaneously allows ohmic contact to n-Ge and p-Ge, because hot carriers circumvent the Schottky barrier formed at metal/n-Ge interfaces. A 2.5× improvement in contact resistivity is reported over previous techniques to achieve ohmic contact to both n- and p-semiconductor. Ohmic contacts at 4.2 K confirm nonequilibrium current transport. Self-assembled Au IMFs are strongly orientated to Ge by annealing near the Au/Ge eutectic temperature. Au IMF nanostructures form, provided the Au layer is below a critical thickness. We anticipate that optimized IMF contacts may have applicability to many material systems. Optimizing this new paradigm for metal−semiconductor contacts offers the prospect of improved nanoelectronic systems and the study of voltage controlled hot holes and electrons.

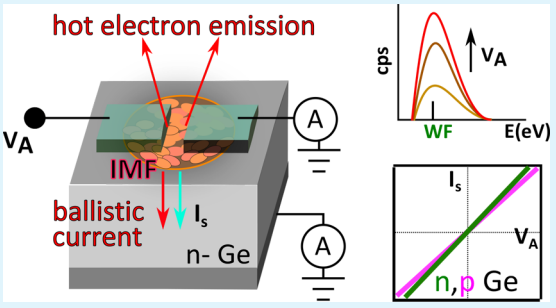

KEYWORDS: *hot carriers, voltage controlled, island metal film, ambipolar contact, Au−Ge, ohmic, ballistic emission, heteroepitaxy*

INTRODUCTION

Good ohmic contacts to semiconductors are vital for electronic devices and systems. Large area contacts or heavy doping are commonly used to achieve this, but are not viable at nanoscale dimensions.[1] Fermi-level depinning using nanoscale interlayers has also been explored, but improved contact to n- semiconductor is at the expense of a high resistance p-contact, or vice versa. The lowest value of specific contact resistivity (ρ_C) for n-Ge using heavy doped interlayers[2] is 1×10^{-7} ohm cm^2, with other reports of quasi-ohmic behavior closer to $\rho_C \approx 1 \times 10^{-5}$ ohm cm^2 using ZnO and TiO_2 interlayers.[2,3] The corresponding increases in contact resistance to p-Ge are not reported.

Embedded metal nanoparticle contact schemes have been demonstrated to modulate the conductivity of metal/semiconductor contacts[4−6] by exploiting field enhancement at nanoparticle/metal/semiconductor triple interfaces. However, these reports show only quasi-ohmic contacts on low doped semiconductors and require heavy doping to achieve usable ohmic contact. To date, 0.02 ohm cm^2 for n-Ge-doped 1×10^{20} cm^{-3} is the lowest reported zero bias contact resistivity (on-state resistance) using this method.[5]

For a metal/semiconductor contact, the sum of electron and hole Schottky barrier heights (Φ_B) is generally equal to the band gap of the semiconductor.[7] Workfunction and interface engineering therefore improve electrical contact for electrons at the expense of holes and vice versa.[8,9] Ge is an exemplar, having ohmic contacts for p-Ge and rectifying contacts for n-Ge. Although Ge has superior intrinsic properties compared to Si,[10] its use is hindered by severe Fermi level pinning. For metal-Ge junctions the Fermi level (E_F) is pinned close to the charge neutral level (CNL) ∼ 0.1 eV above the valence band,[11,12] whereas E_F for bulk n-Ge lies above the intrinsic level (E_i) close to the conduction band. Electrons occupy surface states to establish equilibrium, resulting in band bending and carrier inversion below the surface, shown schematically in Figure 1a. Because $E_F < E_i$, n-Ge develops p-type character near the surface. The metal contact forms an effective Schottky barrier nearly equal to the energy bandgap (∼0.6 eV at room temperature), resulting in rectification.[13] For p-Ge, the bulk E_F lies below E_i close to the valence band. Thus, energy bands

Received: May 10, 2017
Accepted: August 7, 2017
Published: August 7, 2017

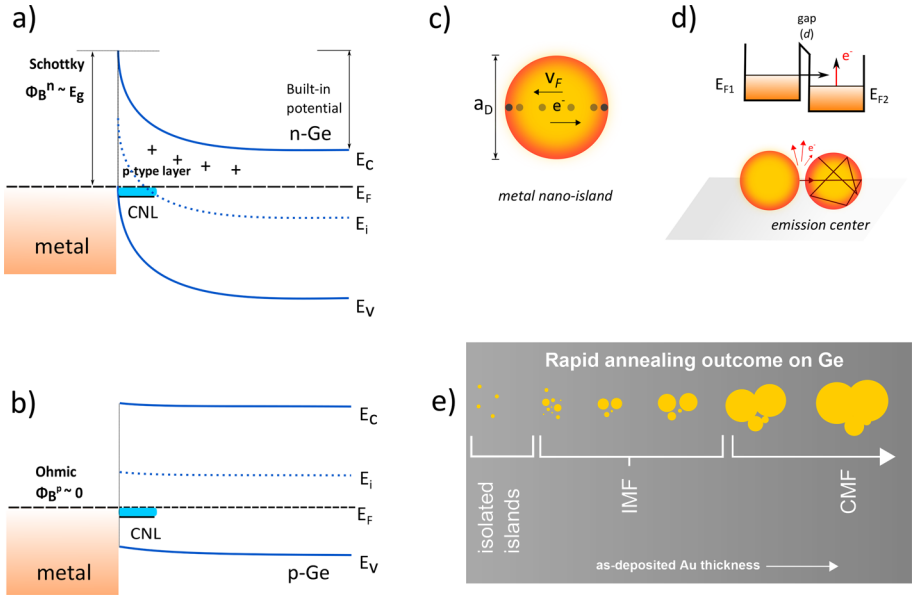

Figure 1. Fermi level pinning in Ge and size effects in metals. (a) Schematic energy band diagram showing typical energetic arrangement of metal/n-Ge contacts where the Schottky barrier formation normally gives a rectifying/Schottky contact. The Fermi level is pinned close to the charge neutral level (CNL) at the surface. The blue shaded region represents occupied acceptor states above the CNL and below E_F (dashed line). A p-type layer beneath the surface fixes the built-in potential, independent of the doping concentration and metal workfunction. (b) Energy band diagram for metal/p-Ge contacts. This arrangement results in ohmic contact due to Fermi level pinning. (c) Ballistic electrons undergo specular/elastic reflections in a metal nanoisland of critical dimensions (a_D) corresponding to the cutoff Debye frequency of the metal. (d) Schematic showing how tunneling current in IMFs causes nonequilibrium electron heating, resulting in hot electron emission. (e) Schematic showing the outcome of rapid annealing on the recrystallized material as the initial Au thickness varies.

are almost flat approaching the surface, resulting in ohmic contact (Figure 1b).

Thermionic emission theory is normally used to characterize electron transport in metal/semiconductor contacts. In a rectifying junction (like metal/n-Ge), only a small fraction of the electrons, described by the high energy tail of the Fermi distribution, can overcome the Schottky barrier. In bulk metals at room temperature, since the average electron temperature is equal to the lattice temperature, this hot electron density is relatively small and results in a low, approximately constant reverse current.

Electron and lattice temperatures reach equilibrium via electron−phonon interactions. For nanoscale metal islands, electron−phonon interactions become limited by the cutoff Debye frequency ($\omega_{D\infty}$) in the phonon spectrum of the metal. Electron motion becomes ballistic in nanostructures having critical dimensions below the electron mean free path. The size limit (a_D) corresponding to $\omega_{D\infty}$ is sketched schematically for the case of a metal nanoisland in Figure 1c. A network of such closely spaced metal islands separated by gaps $d < 5$ nm constitutes an island metal film (IMF). A simple case is shown schematically in Figure 1d. for two metal nanoislands. Under bias, tunneling electrons arriving at the right-hand metal nanoisland undergo electron−electron interactions, allowing nonequilibrium electron heating that will significantly broaden the Fermi distribution of electrons, giving rise to hot electrons and holes. Groups of such closely spaced metal islands behave as hot electron emission centers.[14] Therefore, when a sufficient potential difference is applied to the IMF, hot electrons are emitted from the metal surface into the lowest available energy states in the semiconductor, or into vacuum.

In this letter, we demonstrate that island metal films (IMFs) allow the formation of ohmic contact to semiconductors by hot carrier injection. Au/Ge material is presented here as a model system. There is direct evidence of hot carrier injection from the IMF, which enables ohmic contact to both low and high doped Ge. We investigated metal (IMF)/semiconductor bilayer stack structures, with additional metal contacts patterned on top of the IMF to allow good contact to the IMF.

RESULTS AND DISCUSSION

Photolithography was used to define contact patterns on chemically cleaned n- and p-Ge substrates. Thin Au films of thickness 80−300 nm and a Cr interlayer of thickness 5 nm were deposited by e-beam evaporation. These patterned bilayer contacts were annealed at 400−450 °C, followed by back contact formation (see Methods for details). The contact patterns are relatively large (100−150 μm) compared to the size of the IMF hot electron emission centers formed after annealing (always ≤ initial film thickness). Rapid annealing of thin Au films on Ge above the Au/Ge eutectic temperature (≥360 °C) results in thin film dewetting and cluster formation. With increasing Au film thickness, Figure 1e illustrates the evolution of the recrystallized material from isolated metal islands to IMFs and then to continuous metal film (CMF) like character.

A simple calculation using the cutoff Debye frequency of Au ($\omega_{D\infty}$) ≈ 1×10^{13} Hz and Fermi velocity ($\nu_F \approx 1 \times 10^6$ m/s) shows that $a_D = \frac{\nu_F}{\omega_{D\infty}} \sim 100$ nm. Consequently, nanoparticles smaller than this size would be susceptible to nonequilibrium electron heating effects. Rapid annealing of e-beam evaporated Au thin films (<100 nm thick) on Ge produces small Au clusters but they are separated by gaps too large for tunneling to be an efficient current mechanism. Introducing a thin Cr layer dramatically alters the outcome of annealing. Ensembles of closely spaced nanoislands and nanowires develop within

DOI: 10.1021/acsami.7b06595
ACS Appl. Mater. Interfaces 2017, 9, 27357−27364

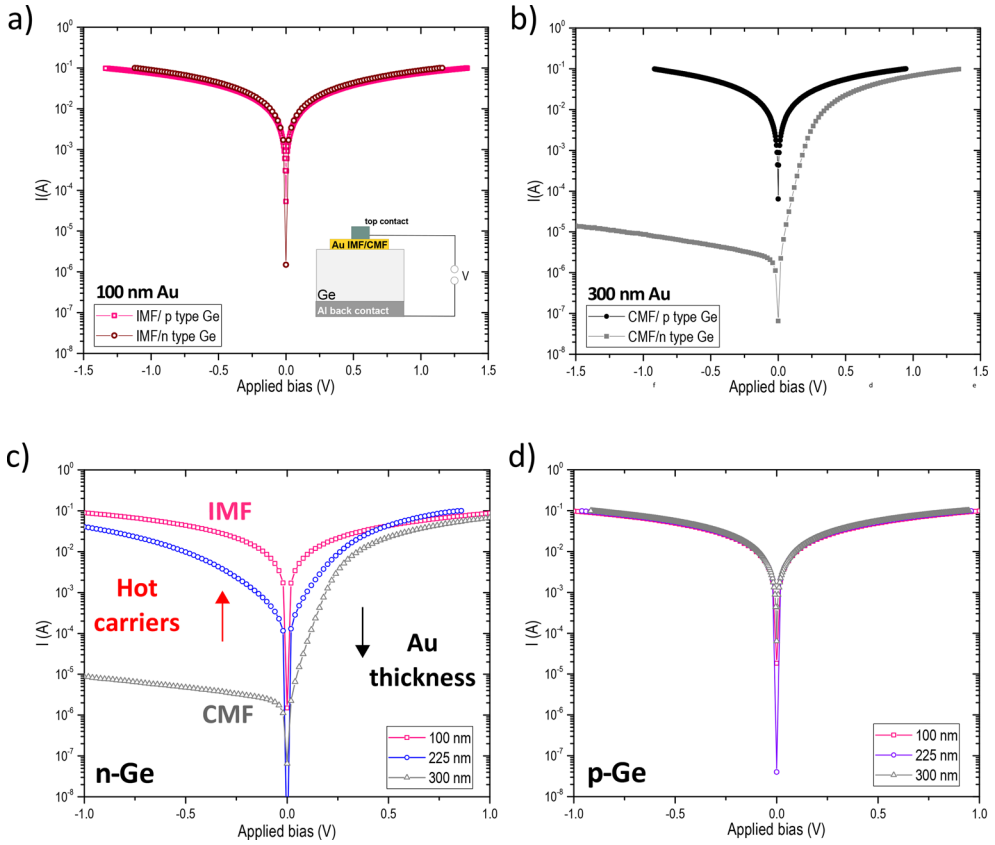

Figure 2. Ohmic contacts to n- and p-Ge ($N_D \approx 1 \times 10^{17}$ cm^{-3} and $N_A \sim 5.6 \times 10^{14}$ cm^{-3}). (a) Room-temperature $I-V$ characteristics of island metal film (IMF) contacts to n- and p-Ge. Inset shows the schematic contact geometry and measurement setup used. Ohmic contact is achieved using the same contact material on both substrates. (b) Room-temperature $I-V$ characteristics of continuous metal film (CMF) contacts to n- and p-Ge. Ohmic characteristics are observed for p-Ge but the contact to n-Ge is rectifying. (c) Hot carrier emission over the n-Ge barrier increases for decreasing as-deposited Au thicknesses, corresponding to a smaller average island size formed after annealing. CMF contacts are rectifying, as expected. (d) Contact to p-Ge is independent of island size / film thickness.

patterned regions on Ge, wherein hot carrier effects are expressed.

Figure 2a shows $I-V$ characteristics when the Au contact is 100 nm thick. The contact to p-Ge shows its expected ohmic characteristics, with symmetric high conductivity under both forward and reverse bias. Extraordinarily, the contact to n-Ge also shows ohmic characteristics using the same metallization scheme. These two curves almost overlap with an on-state resistivity of 0.008 ohm cm^2, comparable to the Ge substrate resistivity and is 2.5× better than the state of the art using metal nanostructures, even though we use lower doped substrates (see Methods). When the Au is 300 nm thick the contact to n-Ge remains rectifying (Figure 2b), which is typical for CMF contacts to n-Ge. The Schottky barrier height for CMF contacts was extracted from high temperature $I-V$ data and found to be ~0.6 eV, consistent with Fermi level pinning in Ge. For intermediate Au thicknesses on n-Ge a gradual change was observed, from the ohmic characteristics using IMFs to the rectifying characteristics using CMFs.

The average metal island size (post-anneal) increases with initial Au film thickness[15] which reduces the number of hot electron emission centers, having dimensions < a_D (~100 nm). This supports the hot electron current hypothesis for reverse current into n-Ge, which reduces with increasing Au film thickness as shown in Figure 2c. The corresponding p-Ge contacts, fabricated with the same Au thicknesses and annealing schedules, remain ohmic throughout the sample series, shown in Figure 2d.

Figure 3a. shows high resolution scanning electron microscope (HRSEM) images of annealed 100 nm thick IMF structure in detail, in comparison with annealed 300 nm Au CMF annealed contact in Figure 3b wherein Au island formation is not observed. HRSEM surveys of the IMF reveal that the larger Au islands have sharp geometric features and are separated by self-similar Au/Ge islands < a_D. (see Figure S1a and Figure S1b for details)

Energy filtered transmission electron microscope (EFTEM) studies showed evidence of Cr migrating to the Au surface due to annealing, effectively encapsulating Au islands (shown in Figure S2). The theta−theta X-ray diffractogram of the Au IMF contact is shown in Figure 3c. The (220)Au is the most intense reflection indicating a preferred orientation with (110)Au planes arranged parallel to the (100)Ge substrate. Electron backscattered diffraction (EBSD) texture scans confirmed that (110)Au crystals were the dominant orientation with some dispersed (111) regions across the contact. Previous demonstrations of heteroepitaxial (110)Au films in the literature have been limited to commensurate epitaxial growth on (110) substrates.[16] Further analysis with an XRD phi-scan measuring the (420)Au plane (Figure 3d) shows clear epitaxial arrangement with peaks occurring every 90° of rotation around the surface normal. (620)Ge substrate contributions to the scan are also seen, offset by 45°. Corroborating field-emission gun

DOI: 10.1021/acsami.7b06595
ACS Appl. Mater. Interfaces 2017, 9, 27357−27364

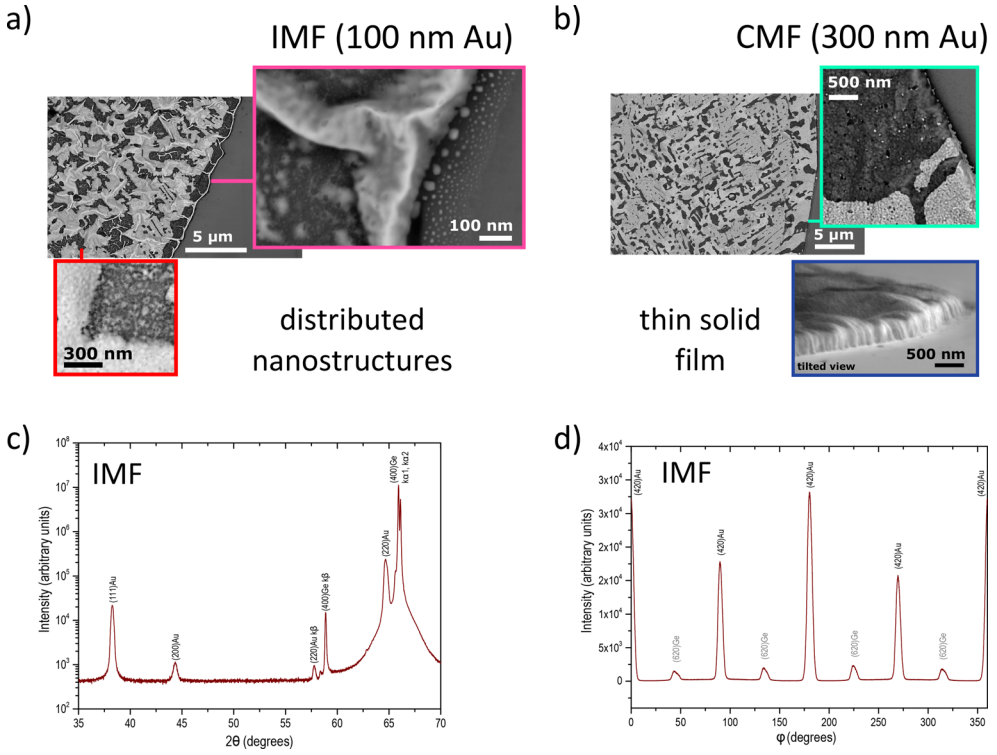

Figure 3. Material structure. (a) Scanning electron microscopy (SEM) images of a 100 nm Au IMF contact. Distributed nanowire and nano-island formations are observed. (b) SEM of a CMF contact showing an electrically continuous film. Nanostructures are absent in the CMF contact. (c) XRD diffractogram of an IMF contact. The intense peak at $2\theta = 65°$ indicates the formation of predominantly (220)Au crystallization. Other identified phases have also been annotated. (d) XRD phi (φ) scan of the (420)Au plane demonstrating the registration of the IMF to the Ge substrate. (620)Ge plane substrate peaks appear offset 45° to the Au signal.

scanning electron microscopy (FEG-SEM)/EBSD analysis (Figure S3a) indicated two strong orientation relationships in the IMF film: [110]Au//[001]Ge and (100)Au//(110)Ge. The small lattice mismatch between the Au FCC unit cell face-diagonals and the Ge lattice parameter (~2% mismatch) allow the formation of this orientation relationship.[17,18]

(110)Au has previously been specified as an ideal medium for hot carrier devices as it offers the highest carrier mean free path (MFP) compared to close-packed (111)Au.[19] A higher MFP is desirable, as it directly influences hot carrier lifetime. This allows the observation of hot carrier effects in relatively large nanostructures (150 nm > initial film thickness >80 nm). Conventional metal-IMF-metal structures use very thin (~10 nm) electroformed metal layers, because thicker films form larger islands upon electroforming and do not demonstrate appreciable hot electron effects due to higher inter-island spacing and smaller carrier mean free path in close packed nanocrystals.

To confirm the hot carrier emission phenomenon in our IMFs, we applied voltage to the metal film laterally, using the electrode array configuration shown in Figure 4a. Emission spectra, shown in Figure 4b, were collected at ambient temperature in vacuo for IMFs and CMFs using a hemispherical electron energy analyzer at various applied biases. Hot electron emission spectra were only observed from the IMF and not from the CMF, as predicted. The corresponding $I-V$ characteristics for this measurement configuration are shown in Figure 4b as an inset. The CMF shows low resistance ohmic characteristics like a bulk metal. The IMF characteristics exhibit relatively high resistance (~33 ohms) below 0.5 V, attributed to tunneling conduction[20] between metal islands. Conductivity increases for higher applied voltage, as the electric field within the nanostructured film becomes sufficiently large for hot electron transport to be the dominant current.

Hot electrons are emitted in this nonlinear regime, at rates increasing with laterally applied bias. Hot electron emissions are not detected from the CMF or from the IMF below 0.5 V. The emission spectra peak near the Au workfunction (5.5 eV) using only small applied biases. These emission data cannot be attributed to field emission but are consistent with the notion of hot electrons emitted from metal nanoislands. The emission distribution appears Maxwellian with effective electron temperature T_e estimated from the variance ($\sigma = kT_e$) in the energy distribution is $\sim 1 \times 10^3$ K. This is typical of previous observations in metal-IMF-metal arrays[14] and comparable with recently reported values for electron fed metal gap junctions.[21]

The electric field corresponding to the onset of hot electron emission into vacuum is estimated from considering Figure 4c, for the IMF region of length L (~10 μm) between the two electrodes. The potential remains constant across metal islands and is assumed to drop lineally between metal islands. If the fraction of IMF which is metal is F_M, the applied potential is V_A, then the electric field strength $\mathbf{E}$ across the IMF is

$$\mathbf{E} = \frac{V_A}{L(1 - F_M)} \quad (1)$$

The minimum voltage for the onset of hot electron emission into vacuum is 0.5 V and it is conservatively assumed that F_M is 0.5. Then the electric field for the onset of hot electron emission is $\sim 1 \times 10^4$ V/cm from eq 1. A comparable electric field is needed vertically through the IMF for the contact, as illustrated in Figure 4d. In this case, the film thickness is ~100

DOI: 10.1021/acsami.7b06595
ACS Appl. Mater. Interfaces 2017, 9, 27357−27364

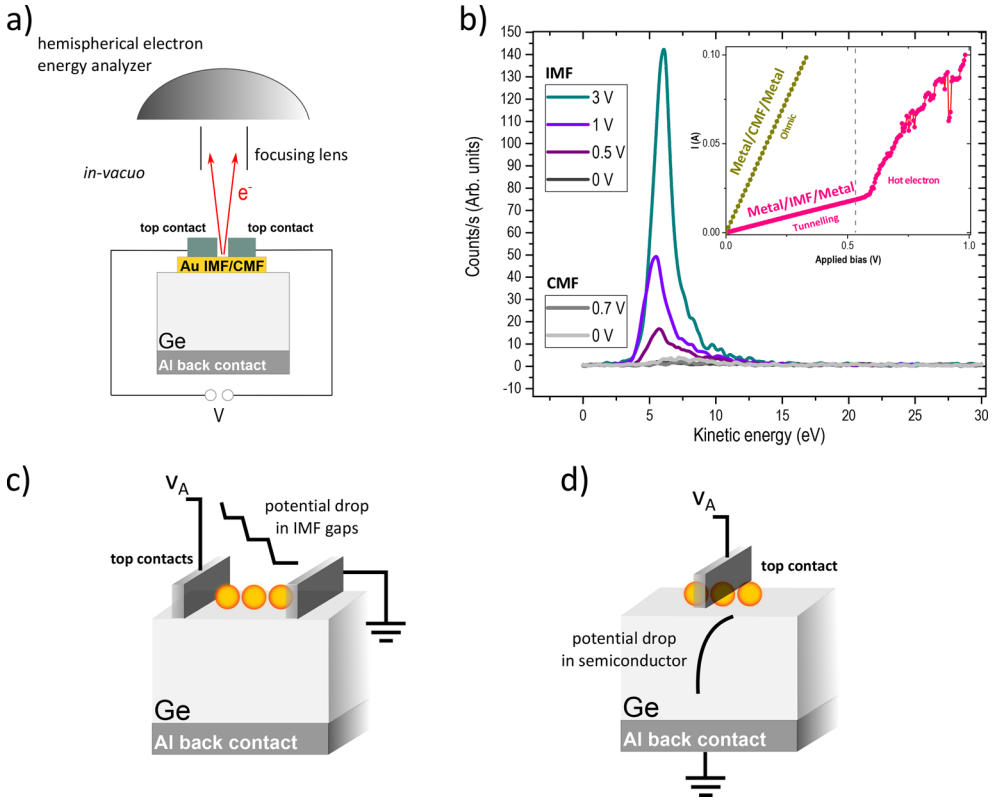

Figure 4. Hot carrier emission from IMFs. (a) Schematic of the experimental setup used to detect hot electron emission into vacuum by laterally biasing a 10 μm region containing IMF or CMF on Ge. (b) Electron emission spectra from IMF and CMF at various applied bias, showing that there is only hot electron emission from the IMF. Inset shows $I-V$ characteristics of the IMF and CMF showing their respective conduction modes. Higher resistance in the IMF case at low voltage is due to tunneling conduction across islands, prior to the onset of hot electron emission. (c) Schematic illustrating potential drop in the IMF for lateral biasing (metal/IMF/metal). (d) Schematic illustrating potential drop in the semiconductor for vertical biasing (IMF/semiconductor), with only mV potential drop needed vertically for hot electron emission into Ge.

nm, and so the corresponding voltage drop across the IMF for the onset of hot electron emission is ~0.5 mV from eq 1.

To better understand the metal/semiconductor ohmic characteristics, IMF and CMF contacts to low doped (6.4×10^{14} cm^{-3}, n$^-$) Ge were investigated. Figure 5a shows these $I-V$ characteristics. The CMF contact to n$^-$ Ge is rectifying, as expected. Using the IMF contact, a high conductivity regime is observed (0.008 ohm cm^2), like that seen at higher doping levels (Figure 2a). An inflection in the $I-V$ curve is seen around −0.6 V, corresponding to a lower conductivity mode (0.03 ohm cm^2). This larger resistance may be due to the wider space charge region in low doped n$^-$ Ge, which has increased from ~100 nm ($N_D \approx 1 \times 10^{17}$ cm^{-3}) to >0.7 μm ($N_D \approx 6.4 \times 10^{14}$ cm^{-3}). Increased hot electron emission at higher bias overcomes this obstacle. The depletion region is effectively charge neutralized by injected electrons and so conductivity increases.[22] Thus, it can be inferred that hot carrier transport observed here is ballistic in nature, shown schematically in Figure 5b. In contrast, the geometry induced electric field enhancement is minimal in a CMF contact. The absence of Au islands eliminates an important pathway for nonequilibrium electron−electron heating in the metal and hence hot carrier transport and hot electron emission into vacuum are not observed.

To further confirm the role of hot carriers in enhancing the conductivity of IMF/semiconductor contacts,we took cryogenic measurements (in liquid helium, 4.2 K) on IMF and CMF/n$^-$-Ge contacts. In Figure 5c, the $I-V$ characteristics using a CMF contact shows negligible current because of carrier freeze out in Ge at 4.2 K. In contrast, by using an IMF contact there is a significant current, which can only be attributed to hot carrier emission from the IMF as cooling to this temperature is detrimental to Fermi level depinning schemes, resulting in rectifying behavior below 111 K[8]. Symmetric $I-V$ characteristics are observed in forward and reverse bias, as was the case at room temperature. The current is small for $-0.1 < V_A < 0.1$, where fewer carriers from the IMF have sufficient energy to inject into the semiconductor. The resistance of the depletion region can be neglected at 4.2 K, which explains why the current magnitude (and conductance) at higher voltages is greater than that seen at room temperature. The current is limited here only by the inversion layer, which the hot carriers easily overcome for $|V_A| > 0.1$ V. The current data can be fitted to a voltage power law (order 2−2.5), which is in qualitative agreement with ballistic electron emission transport across the interface being the main conduction mechanism.[23]

The IMF allows voltage-controlled hot carrier emission into Ge resulting in ohmic characteristics. Under reverse bias, this corresponds with hot electron emission from the IMF into the semiconductor, with sufficient energy to overcome the Schottky barrier in n-Ge. Under forward bias there is a current of similar magnitude to that seen in reverse bias. This must result from hot hole emission from the IMF into the semiconductor. An applied bias across the IMF gives rise to both hot electron and hot hole distributions that rapidly establish an equilibrium.[24] $I-V$ characteristics for the corresponding IMF and CMF contacts

DOI: 10.1021/acsami.7b06595
ACS Appl. Mater. Interfaces 2017, 9, 27357−27364

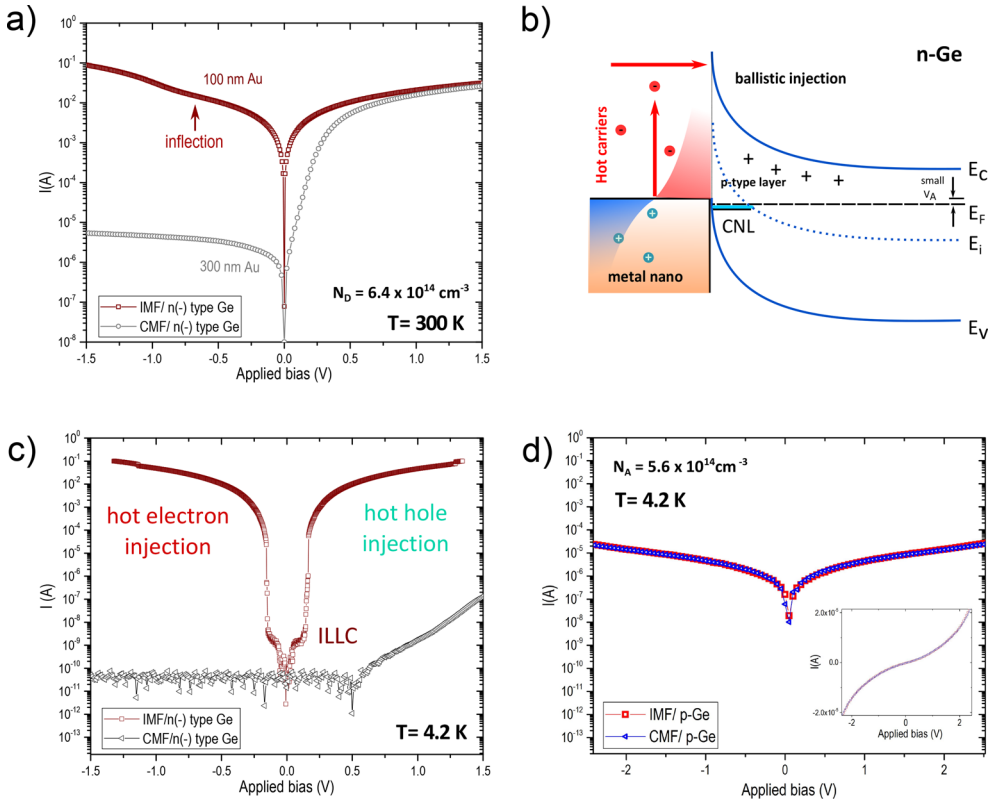

Figure 5. Ballistic hot carrier injection. (a) Room-temperature $I-V$ characteristics of IMF and CMF contacts to low doped n$^-$ Ge ($N_D \approx 6 \times 10^{14}$ cm^{-3}). IMF contact shows high conductivity modes in forward and reverse bias, whereas the CMF contact retains rectifying characteristics. (b) Energy band diagram of IMF/n$^-$ Ge for a small applied reverse bias, resulting in ballistic hot electron injection. (c) Cryogenic (liquid helium, 4.2 K) $I-V$ characteristics of IMF and CMF contacts to low doped n$^-$ Ge. IMF shows symmetric, inversion layer limited current (ILLC) confirming nonequilibrium carrier transport, while CMF contact shows very low current due to the presence of a Schottky barrier and carrier freeze-out. (d) Cryogenic (Liquid helium, 4.2 K) $I-V$ characteristics of IMF and CMF contacts to low doped p Ge ($N_A \sim 5.6 \times 10^{14}$ cm^{-3}). IMF and CMF contact both show identical $I-V$ characteristics. Inset shows the data on a linear scale. A small Schottky barrier for holes allows tunneling near the metal Fermi level, resulting in double exponent $I-V$ characteristics.

to p-Ge taken at 4.2 K are identical, as shown in Figure 5d. Tunneling current is observed, as expected from the condition of Fermi level pinning.

CONCLUSION

Previous IMF studies focused on hot electron emission into vacuum but have not investigated hot carrier injection into semiconductors. Simultaneous hot electron and hot hole emission has been previously demonstrated in artificial photosynthetic devices[25] and separately from sharp metal tips in techniques such as ballistic electron or hole emission microscopy.[26,27] Our work is the first demonstration of voltage controlled IMF/semiconductor contacts that employs both types of charge carriers, resulting in contact resistivity of 0.008 ohm cm^2 for n-Ge-doped 1×10^{17} cm^{-3}, which is 2.5× better than previous results for n-Ge-doped 1×10^{20} cm^{-3}.

These findings are an advance on hot carrier injection into semiconductors resulting from photonic excitation.[28] By using IMFs, hot carriers can be generated electrically, using a low applied voltage and consequently, metal(IMF)/semiconductor junctions become ohmic. The discovery of ohmic contact to a semiconductor by exploiting nanoscale properties of IMFs has important implications. For example, if contact current is mediated by hot carriers injected from the metal then heavily doped semiconductor contacts, with their doping variability at small geometry, are not needed. Poor electrical contact is a particular obstacle to the wider use of Ge, which otherwise has many desirable benefits over Si with reducing geometries. However, if the extrinsic performance of such devices, e.g., nanowire sensors, lags far behind its intrinsic performance because of poor electrical contact, then key benefits may be lost.

METHODS

Sample Preparation (Newcastle University). (100)Ge wafers of n$^-$ (ρ = 2.5–2.7 ohm cm/$N_{D(Sb)} \approx 6.4 \times 10^{14}$ cm^{-3}), n (ρ = 0.029–0.054 ohm cm/$N_{D(Sb)} \approx 1 \times 10^{17}$ cm^{-3}), and p-type (ρ = 0.128–0.5 ohm cm/$N_{A(Ga)} \approx 5.6 \times 10^{14}$ cm^{-3}) conductivity were diced into small rectangular specimens. Samples were blow dried using compressed N_2 before chemical cleaning in organic solvents (Acetone, Isopropyl alcohol [IPA] @ 60 °C) and rinsed repeatedly in deionized (D.I.) water. Following the organic clean, the samples were etched in buffered hydrofluoric acid (BHF) for 90 s and then quenched in D.I. water. Moisture and solvent residues were removed by drying the samples in a fan oven at 120 °C for 60 min. After drying and cooling to ambient temperature, contact patterns of various shapes and dimensions were defined using negative or positive exposure photolithography. The exposed photoresist (AZ 5214-E, Microchemicals) was developed (AZ 326 MIF, Microchemicals) to open contact windows on the substrate. Specimens were rinsed in alternate cycles of D.I. water and BHF (90 s) to remove any oxide or developer residues. The patterned samples were blow dried using compressed N_2 and loaded into the e-beam evaporation chamber, pumped down to high vacuum (1×10^{-7} mbar) using a liquid nitrogen cold trap. Metals were evaporated onto the specimens while monitoring the deposition

DOI: 10.1021/acsami.7b06595
ACS Appl. Mater. Interfaces 2017, 9, 27357–27364

thickness using a quartz crystal microbalance. Five nm of Cr was deposited as an adhesion layer, followed by Au deposition 80 −300 nm. The reason for choosing Au/Cr on Ge is explained in Figure S4. After metal deposition, the contacts were defined by lift-off in warm (60 °C) N-Methyl-2-pyrrolidone (NMP), IPA and rinsing in D.I. water. Specimens were baked at 130 °C for 1 h to evaporate solvent residues and facilitate Cr seeding into Au. Samples were annealed in ultrapure N_2 ambient (200 s.c.c.m.) using a JetFirst 200 benchtop rapid thermal processing (RTP) unit (flush/purge cycles, start/room temperature to 400 °C ramped in 15 s, dwell for 5 s, ramp to 450 °C in 5 s, stop/cooling N_2 purge 500 s.c.c.m. for 240 s). The specimens were cleaned once more in IPA, D.I. water and then the underside was selectively etched in BHF (90 s). After thorough rinsing in D.I. water and drying the samples in N_2 the samples were loaded into an Oxford Instruments PlasmaLab 400 Sputter system in which thick (300 nm) Al back contacts were sputtered onto the sample underside. Additional Ti/Al (20:80) contacts were fabricated onto the films for probing, using photolithography and e-beam evaporation as described previously.

Electrical Measurements (Newcastle University). *I*−*V* characteristics were measured at room temperature using a Keithley 4200 SCS set up to a CASCADE probing station. High resolution dual voltage sweeps, sample and hold setup was used to check for data repeatability and hysteresis.

Electron Emission Spectroscopy (Newcastle University). Electron emission spectra were measured in a Thermo Fisher Scientific Theta Probe X-ray Photoelectron Spectrometer fitted with electrical feed-throughs for in vacuo electrical measurements. Electrical bias was supplied by a Keithley (2600) SMU. Measurements were performed at ambient temperature with a background pressure $<1 \times 10^{-7}$ mbar. The X-ray and flood gun (charge compensation) sources were disabled during acquisition.

Cryogenic Measurements (London low Temperature Laboratory, RHUL). Specimens mounted onto leadless chip carriers and selected contacts were wire bonded before immersing in a bath of liquid helium. *I*−*V* characteristics were measured with a Keithley 2400 SMU. Measurements were repeated with alternating voltage sweep directions to test for hysteresis.

FEG/SEM EBSD, EFTEM, STEM (NiCaL, University of Liverpool). Scanning electron microscope (SEM) images were recorded using a directional backscattered electron detector, fitted to a FEI Helios 600i Dual Beam FIB instrument operating at 5 kV. Electron backscattered diffraction (EBSD) analyses were performed on the same instrument, using an EDAX DigiView EBSD system; data collection and analyses were performed using EDAX OIM software. EBSD was performed on IMF, CMF, and Ge surfaces, tilted 70° to the incident beam, at a working distance of 12 mm. A step size of 100 nm was employed and beam conditions of 20 kV and 11 nA were used.

Electron transparent TEM specimens were produced by the FIB lift out technique. A deposit of carbon was used to protect surface structures before rough milling was performed, using a 30 kV Ga ion beam. A final low energy "wipe" was carried out at 5 kV, to minimize the effects of beam induced surface damage. Bright-field/dark-field scanning transmission electron microscopy (BF/DF-STEM) was carried out in a JEOL 2100FCs probe side aberration corrected instrument operating at 200 kV.

Spatially resolved energy filtered TEM (EFTEM) chemical maps were collected using a Gatan imaging filter (GIF) Quantum SE (model 963), fitted to a JEOL 2100FCs microscope. The microscope was operated in conventional TEM mode, using parallel illumination. The three-window EFTEM technique was employed, with two pre-edge images recorded before the ionization edge (Cr $L_{2,3}$) and one post edge image.

XRD (University of Helsinki). X-ray diffraction (XRD) was measured using Rigaku Smartlab equipped with parallel beam optics. Phi (φ) scans were performed by measuring a rocking curve on (420) Au crystal plane (2θ 115.3°) that is 18.43° tilted with respect to (220) Au plane and recording the maximum intensity with respect to the sample rotation around surface normal. The substrate (620) plane is inclined the exact same tilt angle to the substrate normal with a φ of 45°, and at very close value of 2-theta ($2\theta = 118.8°$) explaining why we see some contribution in the IMF φ scan. The (620)Ge substrate plane φ-scan was also measured to confirm this (measurement included in the Supporting Information, Figure S3.b), and to demonstrate the film/substrate orientation relationship.

■ ASSOCIATED CONTENT

Ⓢ Supporting Information

The Supporting Information is available free of charge on the ACS Publications website at DOI: 10.1021/acsami.7b06595.

HRSEM survey of IMFs and plan view of top contacts, EFTEM showing Cr encapsulation of IMF, EBSD pole figures for orientation relationships of Au IMF and CMF on Ge, metallization sequence selection (PDF)

■ AUTHOR INFORMATION

Corresponding Author

*E-mail: anthony.oneill@ncl.ac.uk.

Author Contributions

†S.G. and P.J.K. contributed equally in conceptualizing the hot carrier mechanism for IMF contacts. A.O. conceived the project. E.A. did early experiments. S.G. developed the material and analyzed the data. K.D. did EFTEM, FEG-SEM/EBSD, and STEM characterization. M.J.H. and P.J.K. did XRD characterization. J.H.Q. did cryogenic *I*−*V* measurements. B.M. and S.G. did electron emission spectroscopy under P.C. S.G., P.J.K., and A.O. wrote the manuscript. All authors contributed to revising the manuscript.

Notes

The authors declare no competing financial interest.

Data supporting this publication is not openly available due to ethical considerations. Access may be possible under appropriate agreement. Additional metadata record at http://dx.doi.org/10.17634/111690-1. Please contact Newcastle Research Data Service at rdm@ncl.ac.uk for further information or access requests.

■ ACKNOWLEDGMENTS

S.G. would like to thank Dr. Konstantin Vasilevskiy, Dr. Jonathan Goss, and Dr. Nikhil Ponon for helpful discussions. This work was funded by the EPSRC (Grant Ref: EP/J010944/1).

■ REFERENCES

(1) Léonard, F.; Talin, A. A. Electrical Contacts to One- and Two-Dimensional Nanomaterials. *Nat. Nanotechnol.* **2011**, *6*, 773−783.

(2) Manik, P. P.; Lodha, S. Contacts on N-Type Germanium Using Variably Doped Zinc Oxide and Highly Doped Indium Tin Oxide Interfacial Layers. *Appl. Phys. Express* **2015**, *8*, 051302.

(3) Kim, G.; Kim, S.; Kim, S.-H.; Park, J.; Seo, Y.; Cho, B. J.; Shin, C.; Shim, J. H.; Yu, H.-Y. Effective Schottky Barrier Height Lowering of Metal/N-Ge with a TiO_2/GeO_2 Interlayer Stack. *ACS Appl. Mater. Interfaces* **2016**, *8*, 35419−35425.

(4) Zheng, H.; Mahajan, B. K.; Su, S. C.; Mukherjee, S.; Gangopadhyay, K.; Gangopadhyay, S. Barrier Modification of Metal-Contact on Silicon by Sub-2 nm Platinum Nanoparticles and Thin Dielectrics. *Sci. Rep.* **2016**, *6*, 25234.

(5) Pavan Kishore, V.; Paramahans, P.; Sadana, S.; Ganguly, U.; Lodha, S. Nanocrystal-Based Ohmic Contacts on N and P-Type Germanium. *Appl. Phys. Lett.* **2012**, *100*, 142107.

(6) Gorji, M. S.; Cheong, K. Y. Embedded Nanoparticles in Schottky and Ohmic Contacts: A Review. *Crit. Rev. Solid State Mater. Sci.* **2015**, *40*, 197−222.

DOI: 10.1021/acsami.7b06595
ACS Appl. Mater. Interfaces 2017, 9, 27357−27364

(7) Balsano, R.; Matsubayashi, A.; LaBella, V. P. Schottky Barrier Height Measurements of Cu/Si(001), Ag/Si(001), and Au/Si(001) Interfaces Utilizing Ballistic Electron Emission Microscopy and Ballistic Hole Emission Microscopy. *AIP Adv.* **2013**, *3*, 112110.
(8) Iyota, M.; Yamamoto, K.; Wang, D.; Yang, H.; Nakashima, H. Ohmic Contact Formation on N-Type Ge by Direct Deposition of TiN. *Appl. Phys. Lett.* **2011**, *98*, 192108.
(9) Nishimura, T.; Kita, K.; Toriumi, A. A Significant Shift of Schottky Barrier Heights at Strongly Pinned Metal/germanium Interface by Inserting an Ultra-Thin Insulating Film. *Appl. Phys. Express* **2008**, *1*, 051406.
(10) Claeys, C. L.; Simoen, E. (Eddy). *Germanium-Based Technologies: From Materials to Devices*; Elsevier: Amsterdam, 2007.
(11) Fowler, A. B. Contact Potential Measurements on Cleaned Germanium Surfaces. *J. Appl. Phys.* **1959**, *30*, 556−558.
(12) Gobeli, G.; Allen, F. Photoelectric Properties and Work Function of Cleaved Germanium Surfaces. *Surf. Sci.* **1964**, *2*, 402−408.
(13) Dimoulas, A.; Tsipas, P.; Sotiropoulos, A.; Evangelou, E. K. Fermi-Level Pinning and Charge Neutrality Level in Germanium. *Appl. Phys. Lett.* **2006**, *89*, 252110.
(14) Fedorovich, R. D.; Naumovets, A. G.; Tomchuk, P. M. Electron and Light Emission from Island Metal Films and Generation of Hot Electrons in Nanoparticles. *Phys. Rep.* **2000**, *328*, 73−179.
(15) Thompson, C. V. Solid-State Dewetting of Thin Films. *Annu. Rev. Mater. Res.* **2012**, *42*, 399−434.
(16) Tolstova, Y.; Omelchenko, S. T.; Shing, A. M.; Atwater, H. A. Heteroepitaxial Growth of Pt and Au Thin Films on MgO Single Crystals by Bias-Assisted Sputtering. *Sci. Rep.* **2016**, *6*, 23232.
(17) Jany, B. R.; Gauquelin, N.; Willhammar, T.; Nikiel, M.; van den Bos, K. H. W.; Janas, A.; Szajna, K.; Verbeeck, J.; Van Aert, S.; Van Tendeloo, G.; et al. Controlled Growth of Hexagonal Gold Nanostructures during Thermally Induced Self-Assembling on Ge(001) Surface. *Sci. Rep.* **2017**, *7*, 42420.
(18) Jung, S. J.; Lutz, T.; Boese, M.; Holmes, J. D.; Boland, J. J. Surface Energy Driven Agglomeration and Growth of Single Crystal Metal Wires. *Nano Lett.* **2011**, *11*, 1294−1299.
(19) Bernardi, M.; Mustafa, J.; Neaton, J. B.; Louie, S. G. Theory and Computation of Hot Carriers Generated by Surface Plasmon Polaritons in Noble Metals. *Nat. Commun.* **2015**, *6*, 7044.
(20) Abeles, B.; Sheng, P.; Coutts, M. D.; Arie, Y. Structural and Electrical Properties of Granular Metal Films. *Adv. Phys.* **1975**, *24*, 407−461.
(21) Buret, M.; Uskov, A. V.; Dellinger, J.; Cazier, N.; Mennemanteuil, M. M.; Berthelot, J.; Smetanin, I. V.; Protsenko, I. E.; Colas-Des-Francs, G.; Bouhelier, A. Spontaneous Hot-Electron Light Emission from Electron-Fed Optical Antennas. *Nano Lett.* **2015**, *15*, 5811−5818.
(22) Fang, Z.; Wang, Y.; Liu, Z.; Schlather, A.; Ajayan, P. M.; Koppens, F. H. L.; Nordlander, P.; Halas, N. J. Plasmon-Induced Doping of Graphene. *ACS Nano* **2012**, *6*, 10222−10228.
(23) Bell, L. D.; Kaiser, W. J. Observation of Interface Band Structure by Ballistic-Electron-Emission Microscopy. *Phys. Rev. Lett.* **1988**, *61*, 2368−2371.
(24) Inouye, H.; Tanaka, K.; Tanahashi, I.; Hirao, K. Ultrafast Dynamics of Nonequilibrium Electrons in a Gold Nanoparticle System. *Phys. Rev. B: Condens. Matter Mater. Phys.* **1998**, *57*, 11334−11340.
(25) Mubeen, S.; Lee, J.; Singh, N.; Krämer, S.; Stucky, G. D.; Moskovits, M. An Autonomous Photosynthetic Device in Which All Charge Carriers Derive from Surface Plasmons. *Nat. Nanotechnol.* **2013**, *8*, 247−251.
(26) Bell, L. D. New Electron and Hole Spectroscopies Based on Ballistic Electron Emission Microscopy. *J. Vac. Sci. Technol., B: Microelectron. Process. Phenom.* **1991**, *9*, 594.
(27) Banerjee, T.; Haq, E.; Siekman, M. H.; Lodder, J. C.; Jansen, R. Ballistic Hole Emission Microscopy on Metal-Semiconductor Interfaces. *IEEE Trans. Magn.* **2005**, *41*, 2642−2644.
(28) Park, J. Y.; Lee, H.; Renzas, J. R.; Zhang, Y.; Somorjai, G. A. Probing Hot Electron Flow Generated on Pt Nanoparticles with Au/TiO 2 Schottky Diodes during Catalytic CO Oxidation. *Nano Lett.* **2008**, *8*, 2388−2392.

DOI: 10.1021/acsami.7b06595
ACS Appl. Mater. Interfaces 2017, 9, 27357−27364